Ferroelectric phase transitions in epitaxial antiferroelectric PbZrO3 thin films

Pauline Dufour, Thomas Maroutian, Maxime Vallet, Kinnary Patel, André Chanthbouala, Charlotte Jacquemont, Lluis Yedra, Vincent Humbert, Florian Godel, Bin Xu, et al.

Ferroelectric phase transitions in epitaxial antiferroelectric $PbZrO_3$ thin films

Pauline Dufour[1], Thomas Maroutian[2], Maxime Vallet[3,4], Kinnary Patel[5], André Chanthbouala[1], Charlotte Jacquemont[1], Lluis Yedra[3], Vincent Humbert[1], Florian Godel[1], Bin Xu[6], Sergey Prosandeev[5], Laurent Bellaiche[5], Mojca Otoničar[7], Stéphane Fusil[1], Brahim Dkhil[3*], Vincent Garcia[1*]

[1]*Unité Mixte de Physique, CNRS, Thales, Université Paris-Saclay, 91767 Palaiseau, France.*

[2]*Centre de Nanosciences et de Nanotechnologies, CNRS, Université Paris-Saclay, 91120 Palaiseau, France.*

[3]Université Paris-Saclay, CentraleSupélec, CNRS, Laboratoire SPMS, 91190, Gif-sur-Yvette, France.

[4]Université Paris-Saclay, CentraleSupélec, ENS Paris-Saclay, CNRS, LMPS - Laboratoire de Mécanique Paris-Saclay, 91190, Gif-sur-Yvette, France.

[5]*Physics Department and Institute for Nanoscience and Engineering, University of Arkansas, Fayetteville, Arkansas 72701, USA*

[6]*Institute of Theoretical and Applied Physics, Jiangsu Key Laboratory of Thin Films, School of Physical Science and Technology, Soochow University, Suzhou 215006, China*

[7]*Electronic Ceramics Department, Jožef Stefan Institute and Jožef Stefan International Postgraduate School, Jamova 39, Ljubljana 1000, Slovenia*

**e-mail: brahim.dkhil@centralesupelec.fr, vincent.garcia@cnrs-thales.fr*

Abstract

The archetypical antiferroelectric, $PbZrO_3$, is currently attracting a lot of interest but no consensus can be clearly established on the nature of his ground state as well as on the influence of external stimuli over its physical properties. Here, the antiferroelectric state of 45-nm-thick epitaxial thin films of $PbZrO_3$ is established by observing the characteristic structural periodicity of antiparallel dipoles at the atomic scale, combined with clear double hysteresis of the polarization-electric field response related to antiferroelectric–to–ferroelectric phase transitions. Surprisingly, while the antiferroelectric state is identified as the ground state, temperature-dependent measurements show that a transition to a ferroelectric-like state appears in a large temperature window (100 K). Atomistic simulations further confirm the existence, and provides the origin, of such ferroelectric state in the films. Electric-field-induced ferroelectric transitions are also detected by the divergence of the piezoresponse force microscopy response. Using this technique, we further reveal the signature of a ferroelectric ground state for 4-nm-thick $PbZrO_3$ films. Compared to bulk crystals, these results suggest a more complex competition between ferroelectric and antiferroelectric phases in epitaxial thin films of $PbZrO_3$.

Introduction

From their first description by Kittel in 1951,[1] the definition of antiferroelectrics has aroused numerous debates, even up to date.[2,3] It is generally admitted that two main features need to be gathered to establish a material as antiferroelectric: on the one hand, an antipolar crystal organization and, on the other hand, the existence of a polar phase close in energy and reachable by application of an electric field.[2,4] This latter feature is paramount for key applications involving antiferroelectricity. Indeed, the peculiar shape of the double hysteresis of polarization vs. electric field results from the volatile transition from an antiferroelectric (AFE) to a ferroelectric (FE) state and propels antiferroelectrics towards high-energy storage capacitors,[5] high-strain actuators,[6] electrocaloric[7,8] and photovoltaic[9] devices. Controlling the stability of the AFE state with respect to the FE one in thin films appears then as the cornerstone for the future integration of such materials into devices.

Among antiferroelectric materials, perovskite lead zirconate, $PbZrO_3$, is probably the most studied. In its bulk form, $PbZrO_3$ undergoes a first-order phase transition from an antiferroelectric phase with a *Pbam* orthorhombic symmetry to a paraelectric phase with a cubic symmetry at a critical temperature of 505 K.[10] This phase transition, which nature is still unclear,[11,12] is accompanied by a divergence of the dielectric susceptibility, as commonly observed for ferroelectric to paraelectric phase transitions.[1,10] Moreover, several reports mentioned the existence of an intermediate ferroelectric phase with a rhombohedral symmetry, detected in a small temperature interval (495-505 K).[13–18] In thick $PbZrO_3$ films (900 nm) fabricated by sol-gel methods, this intermediate ferroelectric phase has also been revealed and its temperature stability could be expanded by an external electric field.[19] Besides, in epitaxial $PbZrO_3$ thin films, the room-temperature stabilization of a pure antiferroelectric phase turned out to be more controversial, with earlier reports on either purely ferroelectric films[20] or mixed antiferroelectric–ferroelectric films.[21] In turn, it was theoretically established that epitaxial strain would affect the competition between the AFE and FE phases.[22] Note that Pb-based thin films have been investigated by first-principle techniques for over twenty years.[22–27] Furthermore, calculations without strain showed that surface effects promote the stabilization of a FE phase below

a critical thickness of 7 nm.[26] Experimentally, a thickness-driven phase transition was detected in epitaxial $PbZrO_3$ thin films[28,29] or superlattices,[30] with critical thicknesses ranging from 8 to 22 nm. However, tunnel transport measurements suggested an antiferroelectric state down to 4 nm $PbZrO_3$ thickness.[31] Moreover, tuning lead stoichiometry in 50-nm-thick epitaxial thin films of $PbZrO_3$ was demonstrated to turn the room-temperature ground state from antiferroelectric to ferroelectric thanks to the incorporation of Pb_{Zr} antisite defects.[32]

Here, combining structural and polarization measurements, we report the room-temperature stabilization of pure antiferroelectric epitaxial thin films of $PbZrO_3$ with thicknesses under 50 nm. We observe a ferroelectric-like state in ultrathin films of 4 nm. Next, we investigate the temperature dependence of the antiferroelectric properties of 45-nm films and reveal a transition to a ferroelectric-like state over a large temperature window (100 K), whose polar configuration is revealed at the atomic scale using scanning transmission electron microscopy. Such surprising polar state is also further evidenced by first-principle-based simulations, which point out the role of epitaxial strain for its emergence in the thin films.

Results and discussion

Structural characterizations. In its bulk antiferroelectric phase, $PbZrO_3$ crystallizes with an orthorhombic symmetry with a = 5.882 Å , b = 11.783 Å and c = 8.228 Å.[33] In the following, we use the subscripts 'o' and 'pc' to define the orthorhombic and pseudo-cubic symmetries, respectively. $PbZrO_3$ thin films were grown by pulsed laser deposition on orthorhombic $GdScO_3(110)_o$ single crystal substrates using a KrF excimer laser. A lead-enriched $Pb_{1.1}ZrO_3$ home-made ceramic target was used for pulsed laser deposition (Supplementary Material). To enable electric-field measurements, we resorted to pseudo-cubic $Ba_{0.5}Sr_{0.5}RuO_3$ thin films as bottom oxide electrodes. Figure 1a shows a typical 2θ-ω X-ray diffraction scan of a typical $PbZrO_3$ (45 nm) / $Ba_{0.5}Sr_{0.5}RuO_3$ (38 nm) bilayer grown on $GdScO_3(110)_o$.

The films do not show any peaks of parasitic phases and display two peaks at 43.95° and 43.57°, corresponding to the $(004)_o$ and $(240)_o$ planes of the orthorhombic crystal symmetry, respectively. These two possible $(001)_o$ and $(120)_o$ epitaxial orientations for $PbZrO_3$, with the corresponding $[001]_o$ and $[210]_o$ growth directions, (sketches in Figure 1b) have been reported in the literature.[21,34] The c parameter, inferred from the position of the $(004)_o$ peak, is estimated to 8.23±0.01 Å, which is in good agreement with the bulk orthorhombic value.[33] In order to investigate the in-plane epitaxial strain, reciprocal space mappings were performed around the $(240)_o$ and $(33\text{-}2)_o$ planes of the $GdScO_3$ substrate (Figure 1c-d). While the bottom electrode of $Ba_{0.5}Sr_{0.5}RuO_3$ appears fully strained on $GdScO_3$, the in-plane reciprocal lattice of $PbZrO_3$ strongly deviates from that of the substrate.

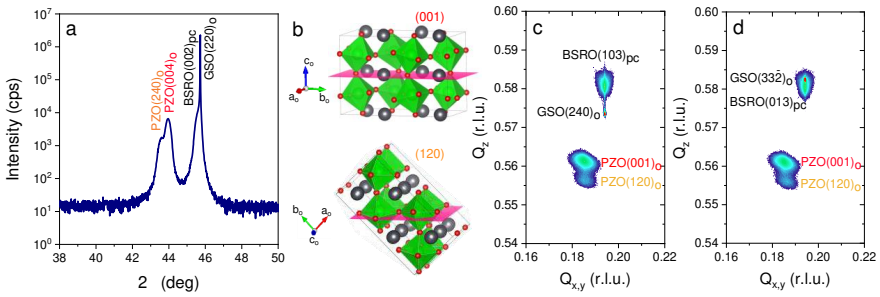

FIG. 1. Structural characterizations of a 45-nm-thick $PbZrO_3$ film grown on $Ba_{0.5}Sr_{0.5}RuO_3$-buffered $GdScO_3$ $(110)_o$. (a) 2θ-ω X-ray diffraction scan showing two peaks related to different orientations of $PbZrO_3$. (b) Sketch of the two possible epitaxial orientations of $PbZrO_3$. The pink planes represent $(001)_o$ and $(120)_o$ basal planes, oriented perpendicular to the growth direction. (c-d) Reciprocal space maps of $(240)_o$ (c) and $(33\text{-}2)_o$ (d) peaks of $GdScO_3$. PZO, BSRO and GSO stand for $PbZrO_3$, $Ba_{0.5}Sr_{0.5}RuO_3$ and $GdScO_3$, respectively. As there are four in-plane variants for the $PbZrO_3$, the peak indices have not been marked in (c) and (d) but replaced by the film orientation they are referred to instead (see Supplementary Material).

To complete the structural analysis of these samples, we used high-angle annular dark field scanning transmission electron microscopy (HAADF-STEM) cross section analysis along two zone axes of the $GdScO_3(110)_o$ substrate (Figure 2). Over these large scale (> 500 nm) specimens, the $PbZrO_3$ film appears well crystallized and continuous. Using image filtering with selected area electron diffraction (SAED), we were able to identify four variants of the $PbZrO_3(120)_o$ domains with 90° in-plane rotations (Figure 2c), with domain sizes varying typically between 10 nm and 50 nm. From the reciprocal space maps, a residual average in-plane strain of -0.05% for $(001)_o$ and +0.13% for $(120)_o$ is estimated in the $PbZrO_3$ thin film, with respect to the bulk value (Supplementary Material). The larger signal of the spots associated to the $(001)_o$ orientation, with respect to the spots of the $(120)_o$ orientation, suggests the predominance of $(001)_o$-oriented $PbZrO_3$ in this film. Although the distribution of these two possible orientations varies from one sample to another with similar thicknesses, a majority of $(001)_o$ domains is often detected for $PbZrO_3$ on $GdScO_3$.

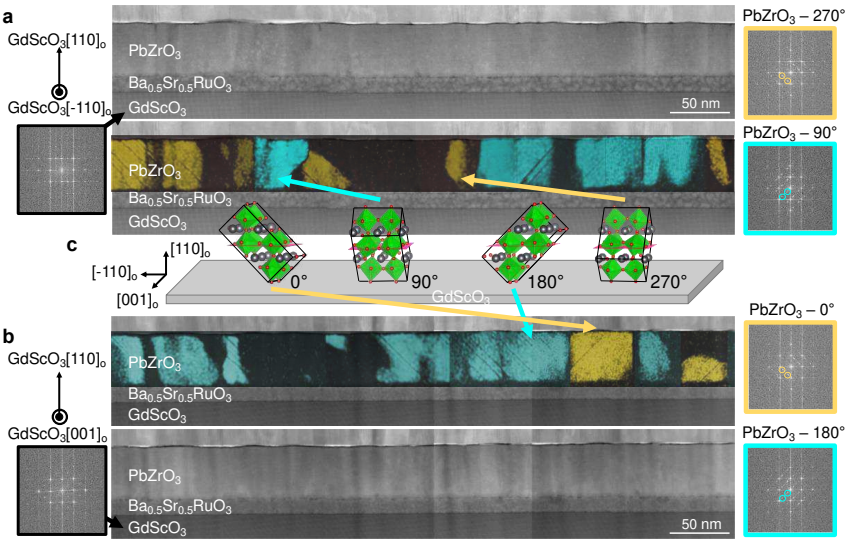

FIG. 2. Room-temperature statistical distribution of the antiferroelectric domains in $PbZrO_3(120)_o$ along the (a) $[1\text{-}10]_o$ and (b) $[001]_o$ zone axes of the $GdScO_3(110)_o$ substrate (see the respective $GdScO_3$

FFTs on the left panels). HAADF-STEM images are displayed for both zone axes and duplicated with highlighted $PbZrO_3$ domains (yellow and blue), as deduced from $PbZrO_3$ FFTs (right panels). (c) Sketch of the four variants of these antiferroelectric domains visible in our films.

Antiferroelectric signatures. To establish the antiferroelectric nature of the $PbZrO_3$ thin films, we investigated the polar displacements and oxygen octahedral tilts at the atomic scale. Cross-sectional images were captured by annular bright field scanning transmission electron microscopy (ABF-STEM). As shown in Figure 1, the $PbZrO_3$ thin films adopt two orientations, $(001)_o$ and $(120)_o$. In the cross-section view of the $(001)_o$-oriented domains, the Pb atoms are periodically displaced within the film plane, meaning their displacements cannot be resolved due to the overlapping of the displaced atoms in the columns. For the $(120)_o$ orientation, however, these antipolar Pb displacements can be detected when the zone axis is parallel to the c axis. The ABF-STEM image in Figure 3a of a $PbZrO_3$ thin film with $(120)_o$ preferential orientation shows a region with two crystallographic domains. On the magnification of the first domain, highlighted in green, and the corresponding simulation (Figure 3b), the displacements of the Pb atoms adopt the typical up-up-down-down antipolar pattern (see large grey dots and arrows), as expected for bulk $PbZrO_3(120)_o$ along the $[001]_o$ zone axis (Figure 3d).[4,35] In the second domain (Figure 3c), highlighted in blue, the staggered atomic displacements along the $[2\text{-}10]_o$ zone axis (Figure 3e) prevent any conclusions on the polarity of this domain. Nevertheless, in this magnified ABF-STEM image we can observe elongated columns at the oxygen positions (red dots), which appear as single spots in the first domain (Figure 3b), indicating anti-phase tilting of the oxygen octahedra. The twinned domains observed along the $[001]_o$ and the $[2\text{-}10]_o$ zone axes are thus 90° oriented domains. Overall, the presence of these twinned nanodomains brings complementary information on the structure of $PbZrO_3$ thin films.

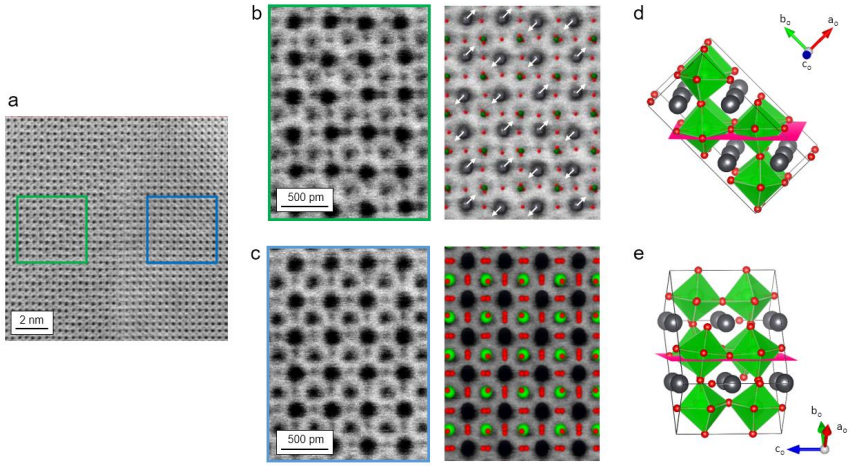

FIG. 3. Atomic scale antiferroelectric features in $PbZrO_3$. (a) Cross-sectional ABF-STEM image of a $PbZrO_3$ thin film showing two domains with different atomic arrangements. (b-c) Magnifications of the two domains delimited by the green (b) and blue (c) squares. The left panels display the raw image and the right panels are overlapped by the simulations of the matching atomic arrangement corresponding to $[001]_o$ (top) and $[2\text{-}10]_o$ (bottom) zone axes, respectively. The white arrows are guides for the eye to underline the antiparallel Pb atom displacements along the $[100]_o$ direction. (d-e) Sketches of the $PbZrO_3$ crystals with the zone axis parallel (d) or perpendicular (e) to the c-axis. In both cases, the $(120)_o$ plane is indicated in pink.

Indeed, the specific arrangement of the oxygen atoms, as visible in the blue domain (Figure 3c), stems from the R mode describing the antiphase rotations of the oxygen octahedra ($a^-a^-c^0$ tilting system).[36] Furthermore, the staggered polarization observed in the green domain (Figure 3b) is a result of the Σ mode. By definition, the two aforementioned modes, which are required to describe the antipolar structure associated to the *Pbam* symmetry of $PbZrO_3$,[11] tend to signify that our $PbZrO_3$ thin films fulfill the structural requirement for an antiferroelectric state. However, these features are not sufficient to certify their antiferroelectric character. Indeed, the reversible transition from an antipolar to a

ferroelectric state by applying an external electric field is required to conclude on the antiferroelectric nature of a material.

To assess the electrical properties, capacitors were fabricated on the $PbZrO_3/Ba_{0.5}Sr_{0.5}RuO_3//GdScO_3$ sample by a combination of optical lithography and lift-off of sputtered Pt top circular electrodes, with diameters varying from 5 to 120 μm. A typical displacement current vs. voltage curve of a 30 μm diameter $Pt/PbZrO_3/Ba_{0.5}Sr_{0.5}RuO_3$ capacitor is shown in Figure 4a. Four clear and sharp switching peaks are observed through this 45-nm-thick $PbZrO_3$ film. The peaks at ± 2.3 V (equivalent to electric fields of 0.5 $MV.cm^{-1}$) correspond to the transition to the ferroelectric phase and the peaks at ± 0.4 V (0.09 $MV.cm^{-1}$) to the switching to the antipolar phase. The associated polarization vs. electric field loop (Figure 4b) exhibits a well-defined double hysteresis, as expected for antiferroelectrics.[37] These electric-field induced ferroelectric phase transitions were further visualized using piezoresponse force microscopy (PFM) through the Pt top electrode of the capacitors (Supplementary Material). While no signal is recorded in the AFE phase, imaging under a dc electric field gives rise to a homogeneous vertical piezoresponse that is switchable by the voltage polarity (Figure 4c, top). Furthermore, the lateral piezoresponse under dc electric field reveals the formation of in-plane domains with submicron sizes (Figure 4c, bottom). As soon as the dc electric field is released, both the vertical and lateral piezoresponses vanish, attesting for a reversible transition to the AFE state. In the electrical measurements as well, we did not detect any contribution from a mixed ferroelectric phase at remanence[21] and the measured remnant polarization of 2.3 $\mu C.cm^{-2}$ may only result from the constant parasitic capacitive contribution vs. voltage (Figure 4a). One remarkable feature of these polarization loops is the very low leakage current at such low film thickness. No significant variations of the polarization loops were observed for capacitor sizes ranging from 5 to 120 μm diameter. In this epitaxial stack, the quality of the interface between the $Ba_{0.5}Sr_{0.5}RuO_3$ bottom electrode and the $GdScO_3$ substrate seems critical to obtain such homogeneous electrical properties. Even though we have reached these high-quality epitaxial films, leakage currents hinder the electrical detection of the AFE-FE transition for films thinner than 45 nm.

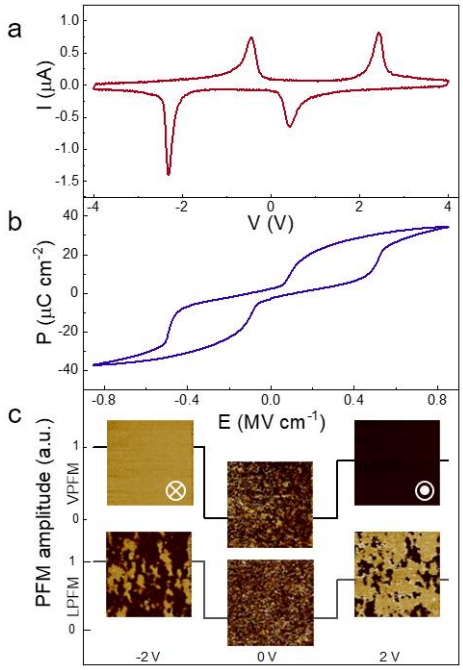

FIG. 4. Electric-field induced ferroelectric phase transitions at room temperature. (a) Current versus voltage loop (I-V) and (b) the corresponding P-E loop. The experiments were performed at 2 kHz. (c) Vertical (top) and lateral (bottom) 3×3 μm^2 PFM phase images recorded under -2 V, 0 V, and +2 V, corresponding to the FE with downward polarization, the AFE, and the FE with upward polarization, respectively. The lateral PFM phase shows domains in the FE state. The normalized PFM amplitudes plotted in the different configurations (continuous lines) exhibit non-zero signals in the FE state and noise levels in the AFE state (see Supplementary Figure 1). VPFM and LPFM stand for vertical and lateral PFM, respectively.

In this section, we use PFM as a powerful tool to complete polarization vs electric field loops. The piezoresponse was recently reported to be proportional to the dielectric susceptibility of antiferroelectric thin films, which diverges at the AFE-FE and FE-AFE transitions.[38] Therefore, by

applying an external electric field, a sharp increase in the piezoresponse is expected at the critical fields observed in the displacement current vs. electric field loops (Figure 5a). We note that, although the I-E loop shown in Figure 4a and Figure 5a are measured on different samples, they display similar properties, underlying the reproducibility of these antiferroelectric devices. An AC voltage of 2 V peak to peak is superimposed to a series of square pulses with incremental amplitudes (right panel of Figure 5b), between the bottom electrode and the PFM probe in contact with the top Pt electrode. Unlike ferroelectrics, antiferroelectrics are not piezoelectric. The PFM signal is thus recorded only in the ON state of the square pulses. Four peaks are detected in the piezoresponse (left panel of Figure 5b), similarly to the I-E loop (Figure 5a). Nevertheless, a shift of the AFE-FE and FE-AFE fields is observed. The AFE-FE transition in the positive bias occurs at 0.46 $MV.cm^{-1}$ on the I-E against 0.29 $MV.cm^{-1}$ with PFM. Similarly, the FE-AFE transition is detected around 0.1 $MV.cm^{-1}$ on the I-E against 0.2 $MV.cm^{-1}$ with PFM. While the I-E loop is acquired at 100 Hz in a dynamic regime, the piezoresponse measurement is performed in a quasi-static regime bouncing back and forth between the ON and OFF states of the rectangular waveform. Therefore, the dynamics might not be fully comparable. The PFM set up was then improved so that the experimental conditions are closer to the I-E loop measurements (right panel of Figure 5c). A triangular waveform is applied with a superimposed AC of 0.3 V peak to peak, oscillating at the PFM resonance frequency in order to amplify the collected signal. This process allows the whole loop to be acquired at 100 Hz, as displayed in Figure 5c. Although the matching is not perfect, the four PFM peaks, corresponding to the phase transitions, approach the ones observed for the I-E loop, bridging both detection methods. It should be note that intrinsic transition field deviations might persist as the I-E loop is collected over the whole capacitor (30 µm diameter) and thus considered as a global measurement. On contrary, the electromechanical response is restricted to the contact area of the PFM probe (few tens of nanometers in diameter). The AC voltage amplitude might also contribute to the shift of the coercive fields. As one may expect, we observed a non-zero piezoresponse for the FE phase and a zero piezoresponse in the AFE phase (Figure 5b-c), in agreement with PFM images with and without electric field (Figure 4c). Despite all the above-mentioned different

measurement conditions, this dynamic PFM technique proves to be of main interest to probe the polar state of ultrathin films, when leakage currents impede the standard electrical approach. Consequently, $PbZrO_3$ thin films of 24 nm and 4 nm were investigated by such dynamic PFM loops. While the 24-nm-thick film exhibits two additional negative peaks (around 0.2 $MV.cm^{-1}$) in its piezoresponse, suggesting a mixed AFE-FE phase (Figure 5d), the 4-nm-thick film displays a butterfly-like shape, mimicking the behavior of ferroelectrics (Figure 5e). Even though piezoresponse properties suggest a polar ferroelectric-like state for 4-nm-thick films, further experiments are still needed. Nevertheless, this observation corroborates the predictions[22] and experimental observations[28–30] of a ferroelectric phase transition below a certain thickness in epitaxial $PbZrO_3$. The stability of the ferroelectric and antiferroelectric phases thus seems to be affected by the so-called size effect.

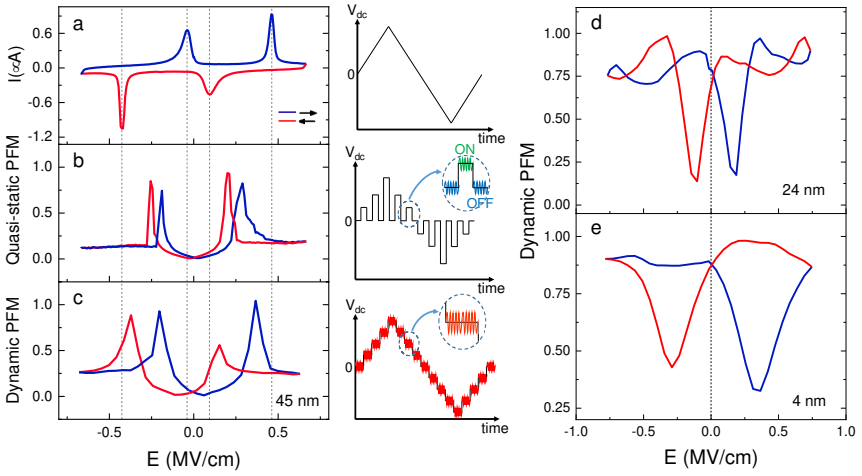

FIG. 5. Electric-field induced antiferroelectric-ferroelectric transitions probed by piezoresponse force microscopy. (a) I-E loop of a 45-nm-thick film collected at 100 Hz. (b) Piezoresponse detected in quasi-static regime on the same sample. (c) Piezoresponse detected in a dynamic regime at 100 Hz. The right panels in (a-c) are sketches of the applied voltage waveforms. From top to bottom: a simple triangular waveform, a series of rectangular waveforms superimposed with an AC voltage (only the ON states are

recorded), and a triangular waveform superimposed with an AC voltage. (d-e) Dynamic electromechanical measurements of two $PbZrO_3$ ultrathin films of 24 nm (d) and 4 nm (e). The blue and red curves in (a-e) account for the voltage scanning directions, as sketched in (a).

Temperature-induced phase transition. After evaluating the stability of the antiferroelectric phase of these epitaxial $PbZrO_3$ thin films when their thickness decreases, we now turn to the influence of temperature. Bulk $PbZrO_3$ undergoes a temperature-driven phase transition from an antiferroelectric state to a paraelectric state at 505 K.[10] However, several reports indicated the existence of an intermediate phase just below the critical temperature.[13,15] Dielectric, Raman spectroscopy, and pyroelectric measurements suggest its ferroelectric nature with a corresponding rhombohedral R3c structure.[14,18,19] Surprisingly, the research to date has no reported such temperature-induced phase transition in $PbZrO_3$ films thinner than 900 nm. Hence, investigating the polar state of this intermediate phase in epitaxial thin films is of importance to establish their phase diagram.

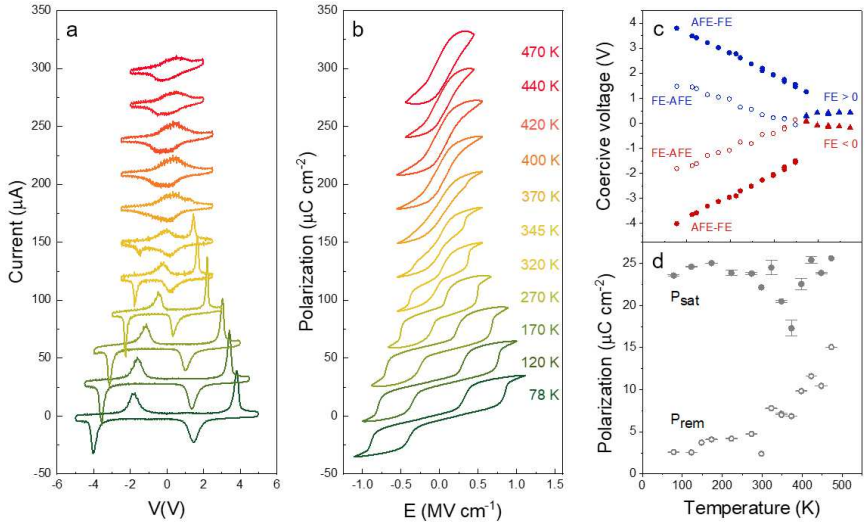

FIG. 6. Electric-field induced phase transitions with increasing temperature. (a-b) I-V and P-E loops of a 45-nm thick $PbZrO_3$ film acquired at several temperatures ranging from 78 K to 470 K at 1 kHz. The I-V and P-E loops are vertically shifted. (c) Evolution of the coercive voltages as a function of temperature. The blue circles correspond to the coercive voltages of the transition from an AFE to a FE state (solid circle) and its associated back-switching (open circle) for positive voltages. The red dots are their equivalent for negative bias. The triangles are the coercive voltages of the ferroelectric-like phase. (d) Temperature evolutions of the remnant polarization (P_{rem}) in solid symbols and of the saturation polarization (P_{sat}) in open symbols.

Electrical measurements are performed from 78 K up to 470 K on the 45-nm-thick $PbZrO_3$ film with a Linkam® set up. The current loops and associated double hysteresis loops are depicted in (Figure 6a-b). Four displacement current peaks can be clearly observed at 78 K (Figure 6a), giving rise to the characteristic double hysteresis loop (Figure 6b). As the temperature increases, these peaks shift to lower voltages and the coercive fields follow a linear evolution in temperature until 370 K (Figure 6c). At 400 K, the four peaks can no longer be detected and only two displacement current peaks are observed, suggesting a destabilization of the antiferroelectricity upon heating and the onset of a ferroelectric-like behavior with the corresponding FE-like P-E loop. Concomitantly with this apparent phase transition, the evolution of the saturation polarization (P_{sat}) shows a singularity around 370 K, while a non-vanishing remnant polarization (P_{rem}) starts increasing around this temperature (Figure 6d). Hence, the $PbZrO_3$ thin film seems to undergo a transition from an antiferroelectric to a ferroelectric-like state at 370-400 K. For temperatures higher than 470 K, the application of the electric field induces some significant leakage contributions accompanied by irreversible changes, preventing the detection of the paraelectric phase transition. This described linear decrease of the coercive fields with temperature was previously reported for 1000 nm thick films, ranging from 333 K to 473 K.[39] In

the case of these 45-nm-thick $PbZrO_3$ films, the onset of ferroelectricity at a lower temperature (370-400 K) could be related to the reduced film thickness.

To gain microscopic insights into the temperature-induced ferroelectric phase transition, we performed in-situ STEM investigations on a similar 45-nm-$PbZrO_3$ thin film as a function of temperature. HAADF-STEM images of the same region of $PbZrO_3$ were taken at five different temperatures while heating from 300 K to 570 K (Figure 7a-e). From the raw images, the displacements of the Pb atoms were estimated by comparing their positions to the barycenter of the four surrounding Zr atoms. The maps of the resulting dipoles are displayed in the bottom panels of Figure 7a-e. The background color scale represents the angular modulation of the dipoles while the vector lengths are proportional to the displacement amplitudes. At 300 K, the dipoles arrange periodically in the form of antiparallel stripes aligned along the $(011)_{pc}$ direction (corresponding to the $(100)_o$ axis) in which each stripe contains two parallel dipole lines (Figure 7a). The 4x unit-cell periodicity, associated with the antipolar arrangement in this orthorhombic structure is confirmed by the $¼\{011\}_{pc}$ superlattice reflections in the electron diffraction pattern (Supplementary Figure 2). It appears that the dipoles are not fully compensated (upward dipoles have a larger amplitude than downward dipoles), in line with recent reports in which the quasi-antiferroelectric state of $PbZrO_3$ displays an amplitude modulation mode or ferrielectric behavior.[29,40,41] Interestingly, this non-compensation can also contribute to the remnant polarization (2.3 $\mu C.cm^{-2}$) we observed in the polarization vs. electric field loop of Figure 4. Note that other contributions such as polar antiphase boundaries,[35] interface compressive strains[42] or localized abundant Pb defects[32] cannot also be completely excluded. The antipolar arrangement remains at 420 K (Figure 7b) and 470 K (Figure 7c) with a gradual decrease of the Pb displacement magnitude when approaching 470 K (see polar plots in the HAADF images). The angle values exhibit two clear populations at 300 K (Figure 7a), and a more dispersive distribution upon heating up to 470 K (Figure 7b-c). At 520 K, a sudden reorganization occurs with mostly parallel displacements pointing in the plane of the film, characterized by an angular modulation close to 0° (Figure 7d). This pseudo-cubic $(010)_{pc}$ direction of the dipoles is not consistent with the commonly accepted rhombohedral

ferroelectric phase of $PbZrO_3$. Instead, it could indicate that this ferroelectric-like phase belongs to a tetragonal-like symmetry.[21,29] On the electron diffraction pattern (Supplementary Figure 2), the typical superlattice reflections of the orthorhombic phase vanish at 520 K. The ferroelectric-like state observed at 520 K disappears at 570 K to make way for a disordered, paraelectric-like, state where the magnitude of the displacement is in the noise range (Figure 7e). To summarize, the polar plots of the Pb displacements highlight these phase transitions as follows: first, a clear distribution in between two opposite orientations at 300 K, then a single polar population at 520 K, and finally an isotropic disordered phase at 570 K (insets of Figure 7a-e). When cooling the specimen down to 300 K, dipoles rearrange in the form of antiparallel stripes, as observed for the initial state (not presented herein).

Overall, the local displacement maps from the STEM measurements (Figure 7) corroborate the electrical measurements (Figure 6), suggesting a temperature-induced phase transition to an intermediate ferroelectric-like phase. We note that the critical temperatures for the ferroelectric phase transition do not perfectly coincide. In the electrical measurements, the ferroelectric-like state appears around 370-400 K while it shows up at 480-520 K in the STEM measurements. A lowering of the AFE-FE transition temperature by 135 K was previously observed in 900 nm-thick $PbZrO_3$ films when an external DC electric field of 0.265 $MV.cm^{-1}$ was applied.[19] Thus, the shift of 115±35 K between electrical measurements and static STEM observations could be ascribed to the electric-field-induced stabilization of the ferroelectric phase in our $PbZrO_3$ films. Indeed, since the free energies of the antiferroelectric and ferroelectric phases are very close, the high electric field required during electrical measurements to switch the dipoles can favor a ferroelectric transition at a lower critical temperature.

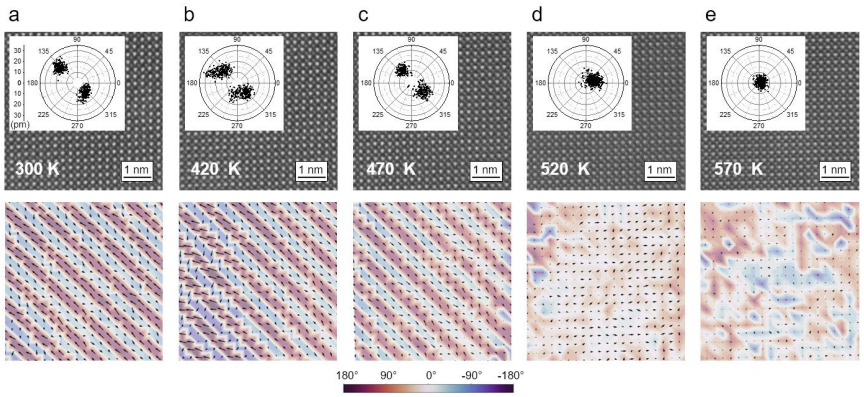

FIG. 7. Temperature-induced phase transition inferred from scanning transmission electron microscopy. (a-e) HAADF-STEM images of the same $PbZrO_3$ domain measured at 300 K (a), 420 K (b), 470 K (c), 520 K (d) and 570 K (e). Insets on the HAADF images display polar plots showing the angle and magnitude distribution of the Pb displacements from their central positions. The bottom panels represent the angle (color scale) and magnitude (vector lengths) modulations of the Pb displacements.

Atomistic simulations based on a first-principle-based effective Hamiltonian scheme provide additional qualitative insight into these temperature-induced phase transitions (see Supplementary Material)[27]. In the case of bulk $PbZrO_3$, this effective Hamiltonian predicts the following structural phases when heating the system from 0 K (Figure 8, top): (1) Phase I (0 – 650 K), which is simply the known *Pbam* ground state of $PbZrO_3$, and that is characterized by three main types of order parameter: an antiphase octahedral tilting about the $(011)_{pc}$ axis ($(100)_o$), along with antiparallel cation displacements along the $(011)_{pc}$ ($(100)_o$) and a complex tilting about the $(100)_{pc}$ axis ($(001)_o$) that are both associated with the Σ point of the cubic first Brillouin zone; (2) Phase II (of *Pbam symmetry too*, 650 – 1300 K), which is deduced from Phase I via the annihilation of the antiphase octahedral tilting about $(011)_{pc}$, and ``only'' possesses Σ -related cation motions along $(011)_{pc}$ and oxygen octahedral tilting about $(100)_{pc}$; (3) Phase III (>1300 K), which is the paraelectric state with cubic P*m-3m* symmetry, and for which all order parameters have vanished. Note that, in Phase II, we numerically found that the lattice parameters are

all close to each other, which may give the impression that this phase is cubic and which thus may explain why it has been overlooked so far (another reason may be that such Phase II exists only on a small local scale in the samples). Effective Hamiltonians are known to qualitatively describe phase transitions' sequence but can provide quantitatively incorrect transition temperatures, as it is the case here for bulk $PbZrO_3$.[43]

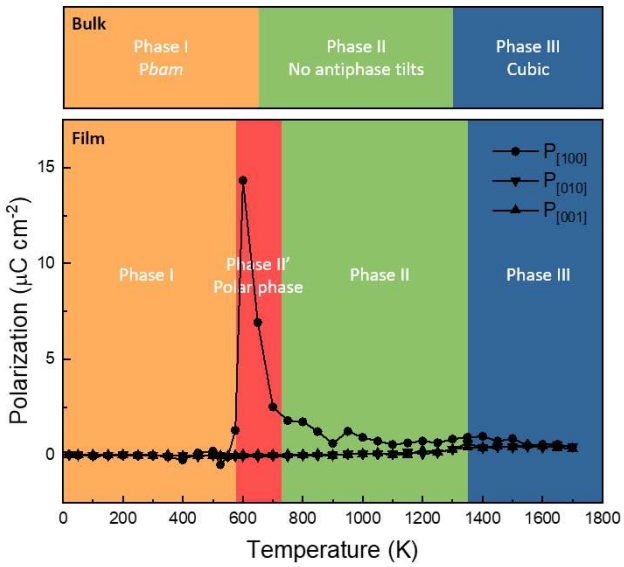

FIG. 8. Computed phase diagram of $PbZrO_3$ using atomistic simulations. Calculated structural phases of $PbZrO_3$ as a function of temperature for bulk (top) and an epitaxial film with fixed in-plane parameters in the $(001)_{pc}$ plane (bottom). The computed polarizations vs. temperature along the in-plane $(100)_{pc}$, $(010)_{pc}$ and out-of-plane $(001)_{pc}$ directions are displayed for the film case (Supplementary Material).

Let us now turn our attention to the case of $PbZrO_3$ films for which we mimic epitaxy with biaxial strain by imposing fixed in-plane lattice constants of about 4.165 Å in the $(001)_{pc}$ plane ($(120)_o$ plane), in

agreement with the experimental values of our $PbZrO_3$ films. Starting from 0 K and increasing the temperature provides the following structural phases (Figure 8, bottom): (i) Phase I (*Pbam*, 0 – 575 K) as in bulk; (ii) Phase II' (P*mc2*$_1$, 575 – 725 K) that looks like bulk Phase II but with the important difference that a ferroelectric polarization now additionally appears along the $(100)_{pc}$ direction in agreement with the polar shifts observed in Figure 7d, with a maximum computed value of about 15 $\mu C.cm^{-2}$ in good agreement with the experimental values (Figure 6); (iii) bulk-like Phase II (*Pbam*, 725 – 1350 K); (iv) Phase III' (paraelectric, >1350 K), similar to Phase III of bulk but with a P*4/mmm* symmetry because of epitaxial conditions.

The predicted existence of the novel *polar* Phase II' in epitaxial thin films and not in the bulk indicates that strain is instrumental to make the ferroelectric polarization we observe along a $(100)_{pc}$ direction to emerge in the films. It is also interesting to realize that this polar phase (i) is predicted to occur at a lower temperature than the Phase I to Phase II bulk transition, in agreement with our experimental demonstrations of a polar phase below the bulk critical temperature; and (ii) has a predicted range of about 150 K, which is rather similar to our measurements providing a 100 K window.

Conclusions

Our work demonstrates direct evidence for antiferroelectric behavior in 45-nm-thick epitaxial $PbZrO_3$ films. The system is found to exhibit a typical double hysteresis loop resulting from the antiferroelectric to ferroelectric electric-field induced transitions as well as the visualizations of an antipolar order at the atomic scale. Reducing the film thickness results in the destabilization of the antiferroelectric state, as revealed by dynamic piezoresponse force microscopy. Finally, we observe a transition to a ferroelectric-like state roughly above 400 K with a wide temperature stability range through temperature-dependent measurements. ~~We observe the transition to a ferroelectric-like state roughly above 400 K with a wide temperature stability range.~~ Atomistic simulations predict that such polar state with P*mc2*$_1$ orthorhombic symmetry arises from epitaxial conditions. Furthermore, the polar displacements associated to this phase suggest a polarization along pseudo-cubic $<100>_{pc}$ directions.

These results open questions on the nature of this electric-field and temperature induced ferroelectric phase in such epitaxial $PbZrO_3$ thin films. In order to exploit the functional properties of this prototypical antiferroelectric, further theoretical investigations are required to shed light on the complex interplay between structure, electric field and temperature.

Acknowledgements

We are grateful to Amr Abdelsamie for carefully reading the manuscript. We thank support from the French Agence Nationale de la Recherche (ANR) through the EXPAND and TATOO (ANR-21-CE09-0033-01) projects, and from the French national network RENATECH for nanofabrication. This work was supported by public grants overseen by the ANR as part of the 'Investissement d'Avenir' programme (ANR-10-LABX-0035 and ANR-10-EQPX-37 MATMECA Grant). This project has received funding from the European Union's Horizon 2020 research and innovation programme under grant agreement No 964931 (TSAR). Proteus funding is acknowledged (grant no. BI-FR/19-20-PROTEUS-009). K.P., S.P. and L.B. are thankful for the Vannevar Bush Faculty Fellowship (VBFF) Grant No. N00014-20-1-2834 from the Department of Defense and the ONR Grant No. N00014-21-1-2086. B.X. acknowledges financial support from Natural Science Foundation of Jiangsu Province (BK20201404).

Supplementary Material

The Supplementary Material contains a description of the methods as well as two Supplementary Figures showing PFM imaging through capacitors under or without electric field (Supplementary Figure 1)and electron diffraction patterns from STEM as a function of temperature (Supplementary Figure 2).

Competing interests

The authors declare no competing interests.

References

[1] C. Kittel, "Theory of Antiferroelectric Crystals," Phys. Rev. **82**(5), 729–732 (1951).
[2] K.M. Rabe, in *Functional Metal Oxides*, edited by S.B. Ogale, T.V. Venkatesan, and M.G. Blamire, 1st ed. (Wiley, 2013), pp. 221–244.
[3] K. Shapovalov, and M. Stengel, "Tilt-driven antiferroelectricity in $PbZrO_3$," (2021).
[4] E. Sawaguchi, H. Maniwa, and S. Hoshino, "Antiferroelectric Structure of Lead Zirconate," Phys. Rev. **83**(5), 1078–1078 (1951).
[5] M. Ye, Q. Sun, X. Chen, Z. Jiang, and F. Wang, "Effect of Eu Doping on the Electrical Properties and Energy Storage Performance of $PbZrO_3$ Antiferroelectric Thin Films," J. Am. Ceram. Soc. **94**(10), 3234–3236 (2011).
[6] S.-T. Zhang, A.B. Kounga, W. Jo, C. Jamin, K. Seifert, T. Granzow, J. Rödel, and D. Damjanovic, "High-Strain Lead-free Antiferroelectric Electrostrictors," Adv. Mater. **21**(46), 4716–4720 (2009).
[7] Y. Liu, J.F. Scott, and B. Dkhil, "Direct and indirect measurements on electrocaloric effect: Recent developments and perspectives," Applied Physics Reviews **3**(3), 031102 (2016).
[8] J. Parui, and S.B. Krupanidhi, "Electrocaloric effect in antiferroelectric $PbZrO_3$ thin films," Phys. Stat. Sol. (RRL) **2**(5), 230–232 (2008).
[9] A. Pérez-Tomás, M. Lira-Cantú, and G. Catalan, "Above-Bandgap Photovoltages in Antiferroelectrics," Adv. Mater. **28**(43), 9644–9647 (2016).
[10] S. Roberts, "Dielectric Properties of Lead Zirconate and Barium-Lead Zirconate," J American Ceramic Society **33**(2), 63–66 (1950).
[11] A.K. Tagantsev, K. Vaideeswaran, S.B. Vakhrushev, A.V. Filimonov, R.G. Burkovsky, A. Shaganov, D. Andronikova, A.I. Rudskoy, A.Q.R. Baron, H. Uchiyama, D. Chernyshov, A. Bosak, Z. Ujma, K. Roleder, A. Majchrowski, J.-H. Ko, and N. Setter, "The origin of antiferroelectricity in $PbZrO_3$," Nat Commun **4**(1), 2229 (2013).
[12] P. Tolédano, and M. Guennou, "Theory of antiferroelectric phase transitions," Phys. Rev. B **94**(1), 014107 (2016).
[13] B.A. Scott, and G. Burns, "Crystal Growth and Observation of the Ferroelectric Phase of $PbZrO_3$," J American Ceramic Society **55**(7), 331–333 (1972).
[14] O.E. Fesenko, R.V. Kolesova, and Yu.G. Sindeyev, "The structural phase transitions in lead zirconate in super-high electric fields," Ferroelectrics **20**(1), 177–178 (1978).
[15] K. Roleder, G.E. Kugel, J. Handerek, M.D. Fontana, C. Carabatos, M. Hafid, and A. Kania, "The first evidence of two phase transitions in $PbZrO_3$ crystals derived from simultaneous raman and dielectric measurements," Ferroelectrics **80**(1), 161–164 (1988).
[16] K. Roleder, and J. Dee, "The defect-induced ferroelectric phase in thin $PbZrO_3$ single crystals," J. Phys.: Condens. Matter **1**(8), 1503–1510 (1989).
[17] Z. Xu, X. Dai, D. Viehland, D.A. Payne, Z. Li, and Y. Jiang, "Ferroelectric Domains and Incommensuration in the Intermediate Phase Region of Lead Zirconate," J American Ceramic Society **78**(8), 2220–2224 (1995).
[18] R. Faye, H. Liu, J.-M. Kiat, B. Dkhil, and P.-E. Janolin, "Non-ergodicity and polar features of the transitional phase in lead zirconate," Appl. Phys. Lett. **105**(16), 162909 (2014).
[19] J. Zhai, and H. Chen, "Direct current field and temperature dependent behaviors of antiferroelectric to ferroelectric switching in highly (100)-oriented PbZrO3 thin films," Appl. Phys. Lett. **82**(16), 2673–2675 (2003).
[20] P. Ayyub, S. Chattopadhyay, R. Pinto, and M.S. Multani, "Ferroelectric behavior in thin films of antiferroelectric materials," Phys. Rev. B **57**(10), R5559–R5562 (1998).
[21] L. Pintilie, K. Boldyreva, M. Alexe, and D. Hesse, "Coexistence of ferroelectricity and antiferroelectricity in epitaxial $PbZrO_3$ films with different orientations," Journal of Applied Physics **103**(2), 024101 (2008).

[22] S.E. Reyes-Lillo, and K.M. Rabe, "Antiferroelectricity and ferroelectricity in epitaxially strained $PbZrO_3$ from first principles," Phys. Rev. B **88**(18), 180102 (2013).
[23] R.I. Eglitis, and D. Vanderbilt, "*Ab initio* calculations of $BaTiO_3$ and $PbTiO_3$ (001) and (011) surface structures," Phys. Rev. B **76**(15), 155439 (2007).
[24] K.M. Rabe, and P. Ghosez, "[No title found]," Journal of Electroceramics **4**(2/3), 379–383 (2000).
[25] J.S. Baker, and D.R. Bowler, "Polar Morphologies from First Principles: $PbTiO_3$ Films on $SrTiO_3$ Substrates and the p(2×Λ) Surface Reconstruction," Adv. Theory Simul. **3**(11), 2000154 (2020).
[26] B.K. Mani, C.-M. Chang, S. Lisenkov, and I. Ponomareva, "Critical Thickness for Antiferroelectricity in $PbZrO_3$," Phys. Rev. Lett. **115**(9), 097601 (2015).
[27] K. Patel, B. Xu, S. Prosandeev, R. Faye, B. Dkhil, P.-E. Janolin, and L. Bellaiche, "A new look at the temperature-dependent properties of the antiferroelectric model $PbZrO_3$: an effective Hamiltonian study," (2022).
[28] A. Roy Chaudhuri, M. Arredondo, A. Hähnel, A. Morelli, M. Becker, M. Alexe, and I. Vrejoiu, "Epitaxial strain stabilization of a ferroelectric phase in $PbZrO_3$ thin films," Phys. Rev. B **84**(5), 054112 (2011).
[29] L. Qiao, C. Song, Q. Wang, Y. Zhou, and F. Pan, "Polarization Evolution in Nanometer-Thick $PbZrO_3$ Films: Implications for Energy Storage and Pyroelectric Sensors," ACS Appl. Nano Mater. **5**(5), 6083–6088 (2022).
[30] K. Boldyreva, L. Pintilie, A. Lotnyk, I.B. Misirlioglu, M. Alexe, and D. Hesse, "Thickness-driven antiferroelectric-to-ferroelectric phase transition of thin $PbZrO_3$ layers in epitaxial $PbZrO_3$/$Pb(Zr_{0.8}Ti_{0.2})O_3$ multilayers," Appl. Phys. Lett. **91**(12), 122915 (2007).
[31] G. Apachitei, J.J.P. Peters, A.M. Sanchez, D.J. Kim, and M. Alexe, "Antiferroelectric Tunnel Junctions," Adv. Electron. Mater. **3**(7), 1700126 (2017).
[32] R. Gao, S.E. Reyes-Lillo, R. Xu, A. Dasgupta, Y. Dong, L.R. Dedon, J. Kim, S. Saremi, Z. Chen, C.R. Serrao, H. Zhou, J.B. Neaton, and L.W. Martin, "Ferroelectricity in $Pb_{1+\delta}ZrO_3$ Thin Films," Chem. Mater. **29**(15), 6544–6551 (2017).
[33] H. Fujishita, and S. Katano, "Crystal structure of perovskite $PbZrO_3$ re-investigated by high resolution powder neutron diffraction," Ferroelectrics **217**(1), 17–20 (1998).
[34] M.P. Moret, J.J. Schermer, F.D. Tichelaar, E. Aret, and P.R. Hageman, "Structure and morphology of epitaxial $PbZrO_3$ films grown by metalorganic chemical vapor deposition," Journal of Applied Physics **92**(7), 3947–3957 (2002).
[35] X.-K. Wei, A.K. Tagantsev, A. Kvasov, K. Roleder, C.-L. Jia, and N. Setter, "Ferroelectric translational antiphase boundaries in nonpolar materials," Nat Commun **5**(1), 3031 (2014).
[36] A.M. Glazer, "The classification of tilted octahedra in perovskites," Acta Crystallogr B Struct Crystallogr Cryst Chem **28**(11), 3384–3392 (1972).
[37] K. Yamakawa, S. Trolier-McKinstry, J.P. Dougherty, and S.B. Krupanidhi, "Reactive magnetron co-sputtered antiferroelectric lead zirconate thin films," Appl. Phys. Lett. **67**(14), 2014–2016 (1995).
[38] Haidong Lu, Sebastjan Glinsek, Pratyush Buragohain, Emmanuel Defay, and Jorge Iñiguez, "Probing Antiferroelectric-Ferroelectric Phase Transitions in $PbZrO_3$ Capacitors by Piezoresponse Force Microscopy," Advanced Functional Materials **2003622**, (2020).
[39] M.D. Nguyen, and G. Rijnders, "Electric field-induced phase transition and energy storage performance of highly-textured $PbZrO_3$ antiferroelectric films with a deposition temperature dependence," Journal of the European Ceramic Society **38**(15), 4953–4961 (2018).
[40] T. Ma, Z. Fan, B. Xu, T.-H. Kim, P. Lu, L. Bellaiche, M.J. Kramer, X. Tan, and L. Zhou, "Uncompensated Polarization in Incommensurate Modulations of Perovskite Antiferroelectrics," Phys. Rev. Lett. **123**(21), 217602 (2019).
[41] Y. Yao, A. Naden, M. Tian, S. Lisenkov, Z. Beller, A. Kumar, J. Kacher, I. Ponomareva, and N. Bassiri-Gharb, "Ferrielectricity in the Archetypal Antiferroelectric, $PbZrO_3$," Advanced Materials **35**(3), 2206541 (2023).
[42] X.-K. Wei, K. Vaideeswaran, C.S. Sandu, C.-L. Jia, and N. Setter, "Preferential Creation of Polar Translational Boundaries by Interface Engineering in Antiferroelectric $PbZrO_3$ Thin Films," Adv. Mater. Interfaces **2**(18), 1500349 (2015).

[43] W. Zhong, D. Vanderbilt, and K.M. Rabe, "First-principles theory of ferroelectric phase transitions for perovskites: The case of $BaTiO_3$," Phys. Rev. B **52**(9), 6301–6312 (1995).
[44] M. Nord, P.E. Vullum, I. MacLaren, T. Tybell, and R. Holmestad, "Atomap: a new software tool for the automated analysis of atomic resolution images using two-dimensional Gaussian fitting," Adv Struct Chem Imag **3**(1), 9 (2017).
[45] E. O'Connell, M. Hennessy, and E. Moynihan, "PinkShnack/TEMUL: Version 0.1.3," (2021).
[46] Y. Yang, B. Xu, C. Xu, W. Ren, and L. Bellaiche, "Understanding and revisiting the most complex perovskite system via atomistic simulations," Phys. Rev. B **97**(17), 174106 (2018).
[47] K. Patel, S. Prosandeev, Y. Yang, B. Xu, J. Íñiguez, and L. Bellaiche, "Atomistic mechanism leading to complex antiferroelectric and incommensurate perovskites," Phys. Rev. B **94**(5), 054107 (2016).

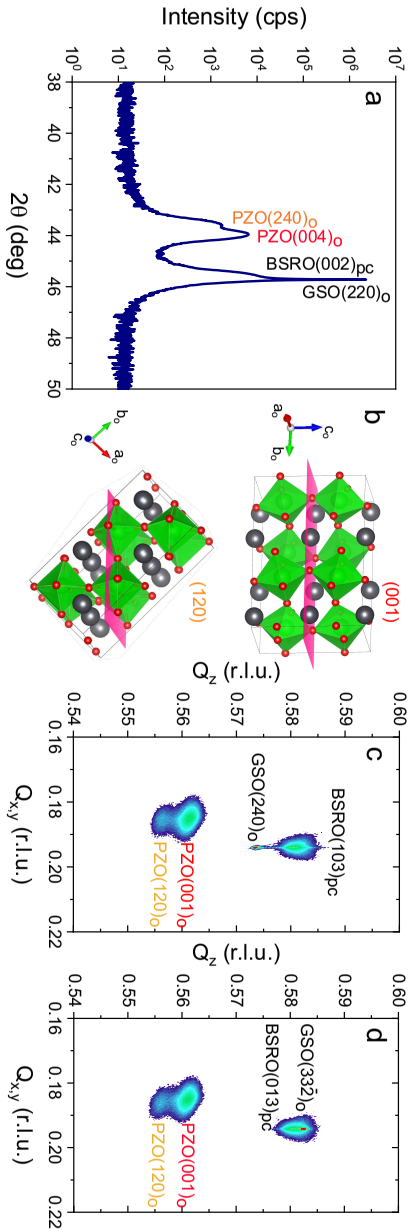

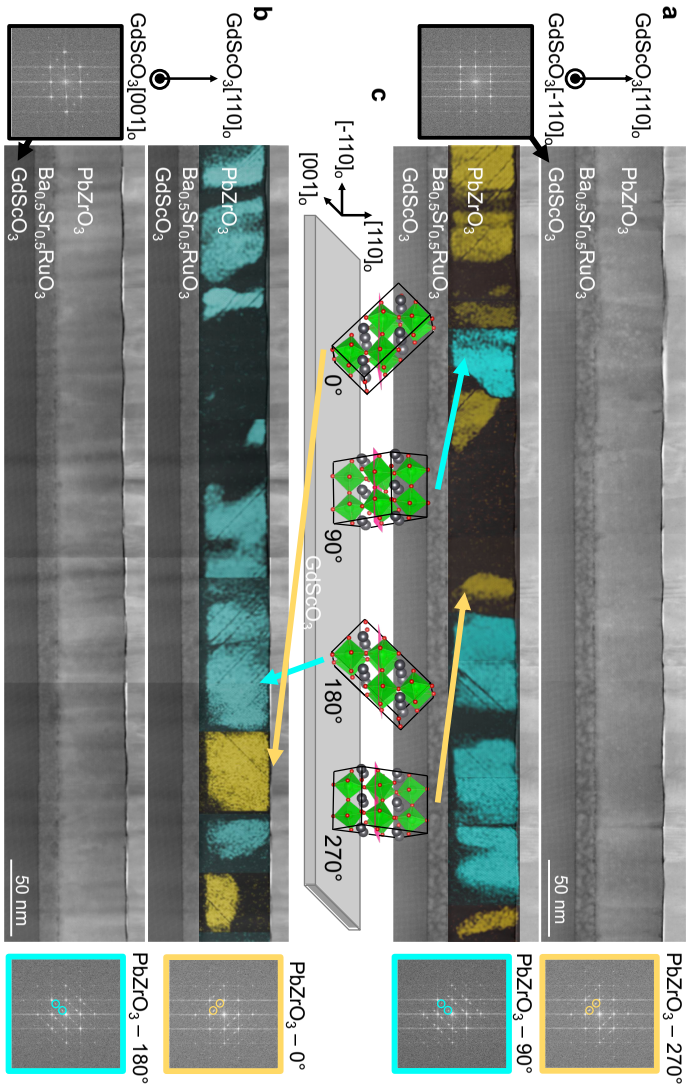

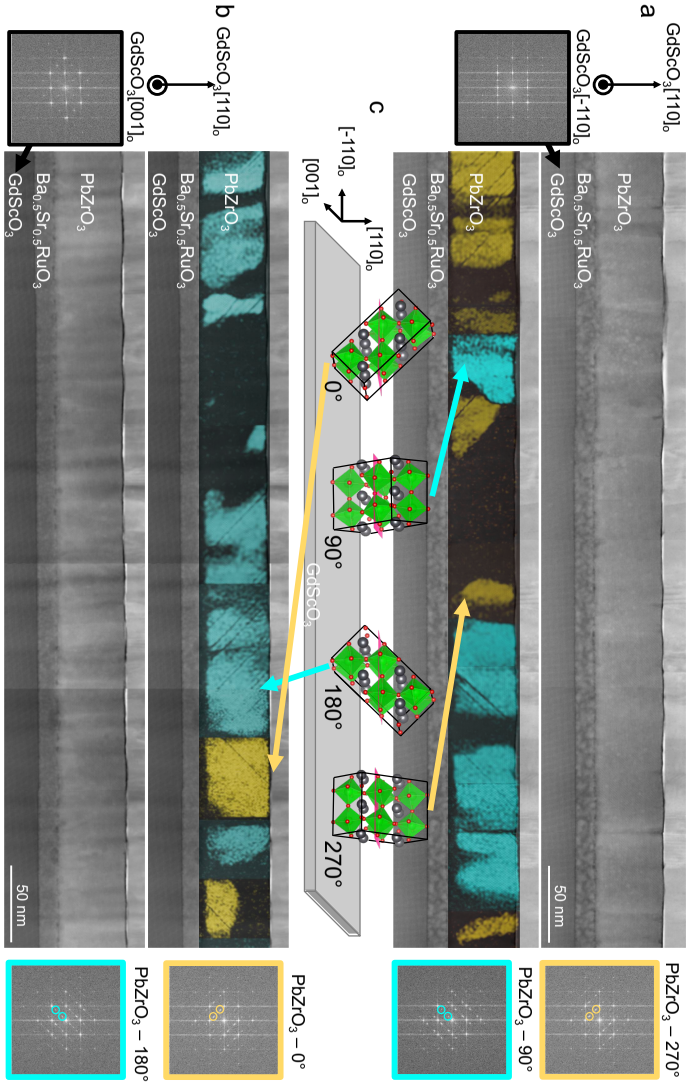

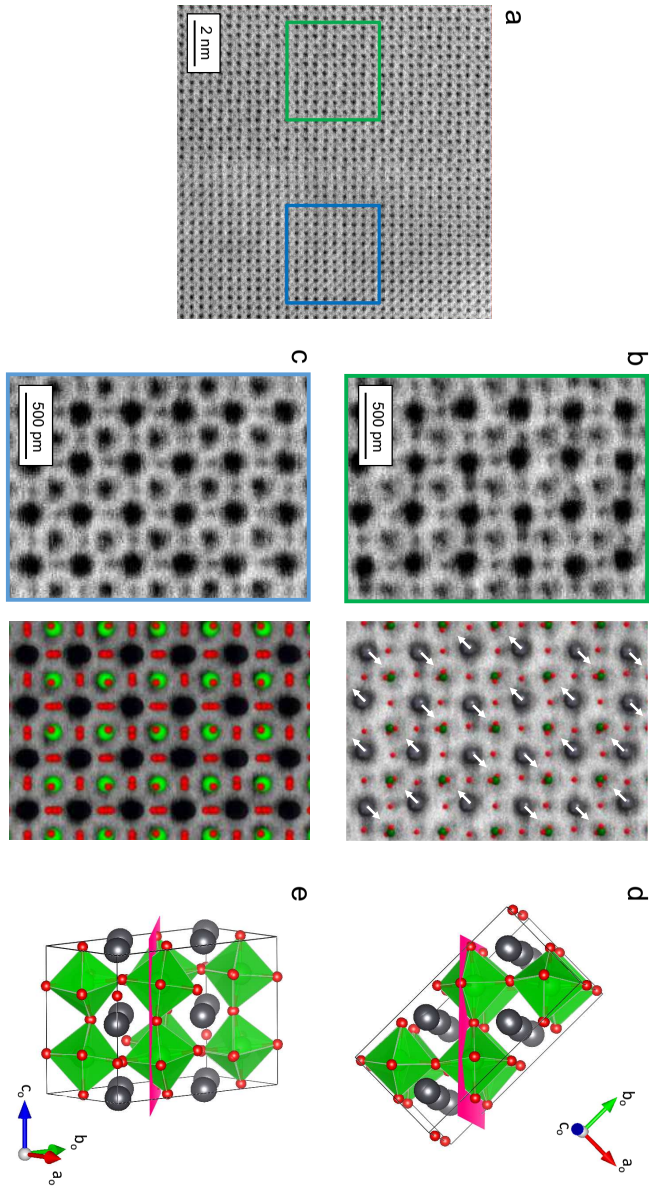

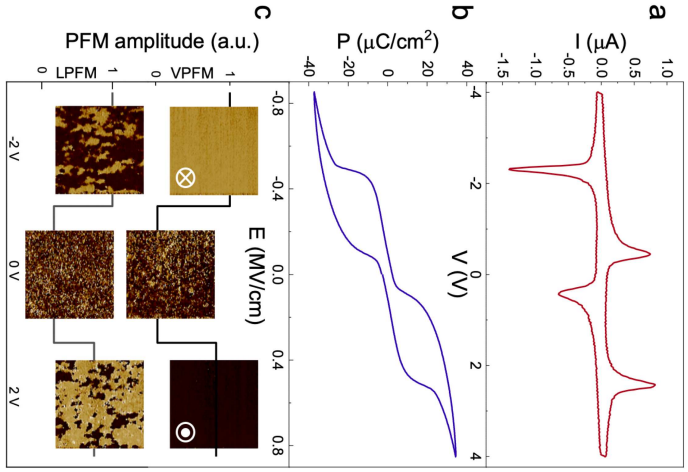

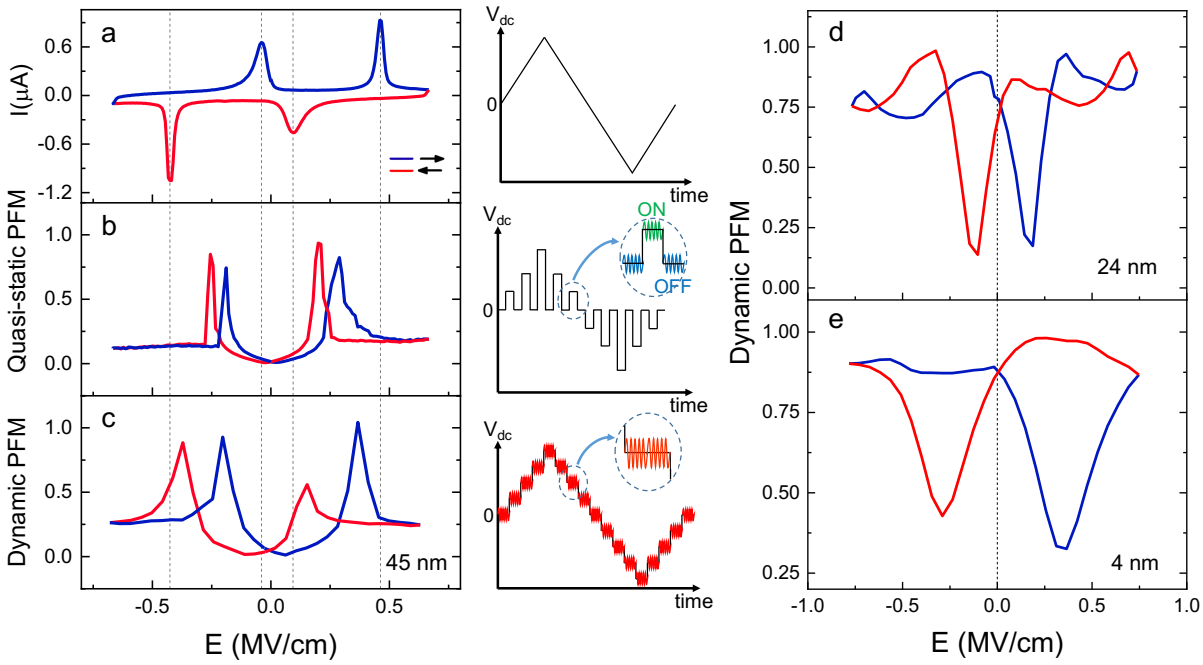

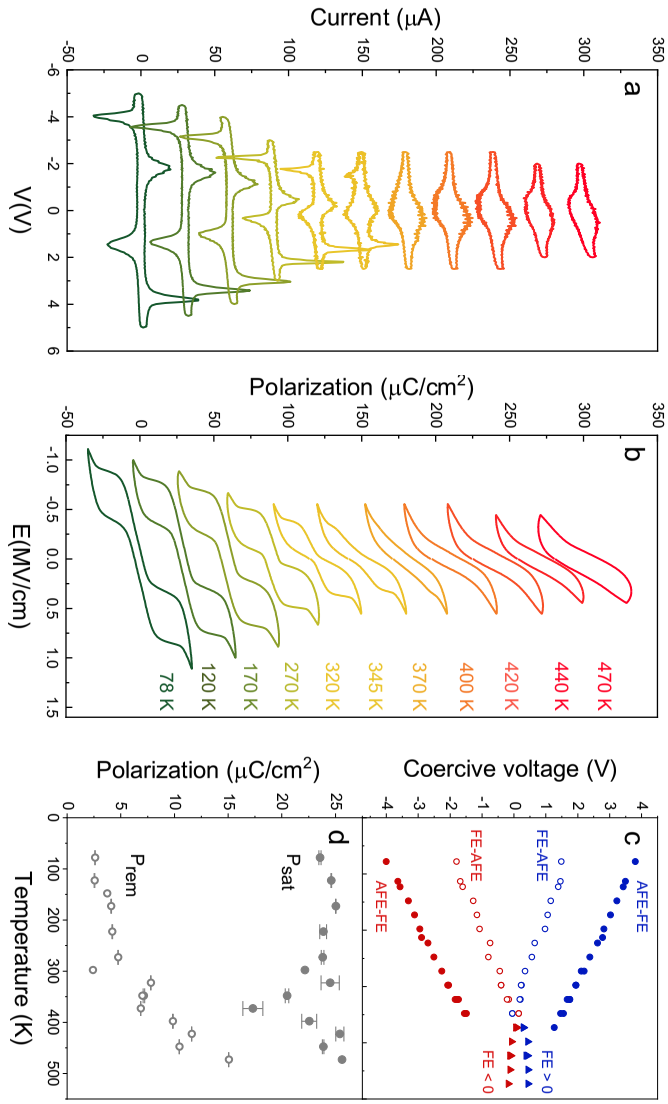

PLEASE CITE THIS ARTICLE AS DOI: 10.1063/5.0143892